SI Appendix

Eisenman and Wettlaufer 10.1073/pnas.0806887106

Here we derive the idealized Arctic sea ice–ocean–atmosphere model that is summarized in equations [1]-[4] of the Research Report. Note that we carry out the entire derivation using dimensional variables, rather than following the conventional mathematical development of such equations through a process of non-dimensionalization, in order to make direct contact with previous studies of the thermodynamics of sea ice and climate.

Sea Ice

The evolution of the sea ice temperature profile is an idealized version of the single-column thermodynamic model of Maykut and Untersteiner (1) (hereafter MU71). Vertical heat conduction in sea ice is computed in MU71 according to

$$c_{\text{eff}}(\tilde{T},S)\frac{\partial \tilde{T}}{\partial t}=\frac{\partial}{\partial z}\left[k_{\text{eff}}(\tilde{T},S)\frac{\partial \tilde{T}}{\partial z}\right]+A_R, \qquad [6]$$

which can be derived from the general theory of mushy layers (2). Here A_R represents the absorption of shortwave radiation that has penetrated below the surface of the ice, the effective heat capacity $c_{\text{eff}}(\tilde{T},S)$ and thermal conductivity $k_{\text{eff}}(\tilde{T},S)$ depend on simulated temperature $\tilde{T}$ and specified salinity S, and the vertical coordinate z increases upward. Note that for the $\tilde{T}$ and S range in perennial ice, MU71 neglect the vertical derivative of the effective conductivity, $\partial k_{\text{eff}}(\tilde{T},S)/\partial z$, allowing the first term on the right-hand side of equation [6] to be expressed as $k_{\text{eff}}(\tilde{T},S)\partial^2\tilde{T}/\partial z^2$. MU71 also include a layer of snow above the ice with specified snowfall and simulated snow melt.

The boundary condition in MU71 at the upper surface ($z=h_T$) is a flux balance when the ice is below the freezing temperature ($\tilde{T}_{fr}$) and otherwise a Stefan condition for surface ablation:

$$\left[k_{\text{eff}}(\tilde{T},S)\frac{\partial \tilde{T}}{\partial z}\right]_{z=h_T}+F_{top}(t,T_i,\alpha_i)=\begin{cases}0 & T_i<0\\ L_i\frac{dh_T}{dt} & T_i=0\end{cases}, \qquad [7]$$

with L_i the latent heat of fusion of ice, α_i the surface albedo, $T_i\equiv\tilde{T}_i-\tilde{T}_{fr}$ the surface temperature departure from the freezing point with $\tilde{T}_i\equiv\tilde{T}(z=h_T)$, and $F_{top}(t,T_i,\alpha_i)$ representing the sum of sensible and latent heat fluxes and longwave and shortwave radiative fluxes out of the surface. The seasonal cycle of each of these components of the surface flux are specified in MU71 based on observations, except for the upward longwave flux which is computed from the surface temperature using the Stefan-Boltzmann equation. To facilitate an analytical solution for T_i (equation [15] below), we approximate the Stefan-Boltzmann equation by its linearized version, $\sigma\tilde{T}_i^4=\sigma_0+\sigma_T T_i$, where σ is the Stefan-Boltzmann constant and the parameters ($\sigma_0=316$ Wm^{-2}, $\sigma_T=3.9$ Wm^{-2}K^{-1}) are chosen such that the equation is exact when $\tilde{T}_i=-30$°C and when $\tilde{T}_i=0$°C, which are the approximate values of $\tilde{T}_i$ during most of the winter and summer, respectively. This allows the temperature dependence of the surface flux to be expressed as

$$F_{top}(t,T_i,\alpha_i)=-(1-\alpha_i)F_S(t)+F_0(t)+F_T(t)T_i, \qquad [8]$$

where $F_S(t)$ is the downwelling shortwave radiation flux, $F_0(t)$ is σ_0 plus the specified sensible and latent heat fluxes, and $F_T(t)=\sigma_T$. Note that here the atmosphere is specified as in MU71, whereas in the full coupled version of the model $F_0(t)$ and $F_T(t)$ take on a different set of values computed using the atmospheric model (equations [39]-[40] below).

At the ice–ocean interface ($z=h_B$), MU71 apply a Stefan condition for ice growth or ablation,

$$-L_i\frac{dh_B}{dt}=-\left[k_{\text{eff}}(\tilde{T},S)\frac{\partial \tilde{T}}{\partial z}\right]_{z=h_B}-F_B, \qquad [9]$$

with the flux from the ocean into the base of the ice specified to take a constant value of $F_B=2$ Wm^{-2}. Note that the temperature at the ice–ocean interface must be at the freezing point, $\tilde{T}(z=h_B)=\tilde{T}_{fr}$. The upper and lower surfaces of the ice, h_T and h_B, evolve separately in MU71, who use a coordinate system in which each ice parcel remains stationary, and the predicted ice thickness is $h_i=h_T-h_B$ (see schematic in Fig. S1).

Here we neglect snow (MU71 report that having no snow causes the annual mean thickness to increase by 17cm from the standard case value of 288cm), and we neglect penetrating shortwave radiation $A_R\to 0$ (which MU71 report causes the annual mean ice thickness to decrease by 45cm). The impact of neglecting both of these factors is shown in Fig. S2 (black curves).

The thermal conductivity $k_{\text{eff}}(\tilde{T},S)$ in the MU71 standard case run is always 90%–100% of the pure ice value, and we approximate it to take the constant pure ice value, $k_{\text{eff}}(\tilde{T},S)=k_i=2$ Wm^{-1}K^{-1}. The freezing temperature in MU71 is taken to be $\tilde{T}_{fr}=-1.8$°C at the base of the ice and $\tilde{T}_{fr}=-0.1$°C at the upper ice surface, and we approximate it to take a constant value of $\tilde{T}_{fr}=0$°C. Lastly, because the Stefan number $N_S\equiv L_i/\left[c_{\text{eff}}(\tilde{T},S)\Delta\tilde{T}\right]$ is large, the temperature field in the ice relaxes quickly in response to changes in the solidification rate. The actual values of N_S predicted by the MU71 standard case seasonal cycle vary widely but typically are $N_S\gg 1$. Under these conditions, the system [6]-[7], [9] can be expressed as a single ordinary differential equation, as described below.

Applying the large Stefan number approximation to the heat conduction equation [6] yields a linear temperature profile, $\tilde{T}=\tilde{T}_{fr}+(\tilde{T}_i-\tilde{T}_{fr})(z-h_B)/(h_T-h_B)=\tilde{T}_{fr}+T_i(z-h_B)/h_i$, which can be derived using a scaling argument after vertically integrating equation [6] and inserting the boundary conditions [7], [9]. Next, this quasi-stationary temperature field is inserted into equations [7], [9]. The upper boundary condition [7] includes two different cases depending on whether or not surface ablation is occurring:

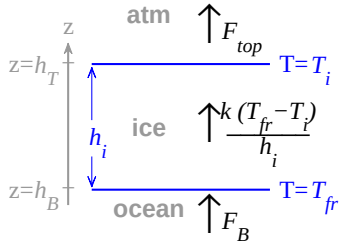

Fig. S1. Schematic showing fluxes and variables in the sea ice component of the idealized model presented here. All fluxes are defined such that a positive value implies an upward flux.

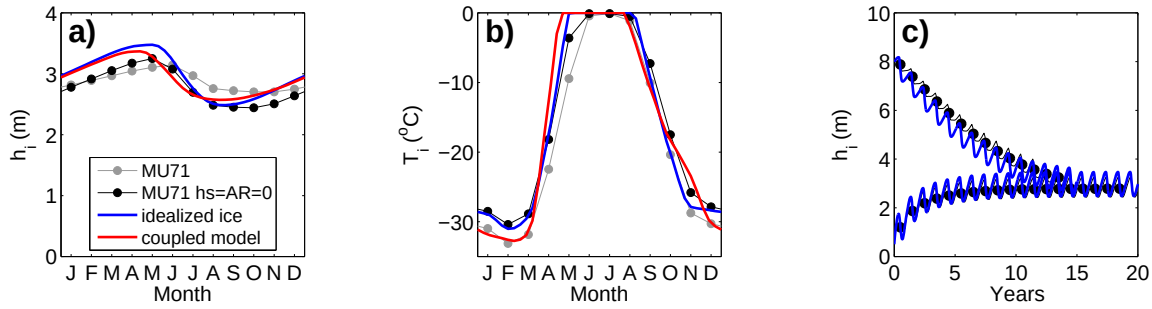

Fig. S2. Effects of approximating the ice thermodynamics in the model of MU71 (1). (a) Steady-state solution seasonal cycle of ice thickness in the MU71 standard case simulation (gray curve and circles), in a simulation with the MU71 model carried out for this study with no snow or penetrating shortwave radiation ($h_s = A_R = 0$; black curve and circles), when the MU71 representation is replaced by the idealized sea ice model given by equations [**15**]-[**16**] (blue curve), and the standard case run with the fully coupled idealized sea ice–ocean–atmosphere model summarized in equations [**1**]-[**4**] of the Research Report (red curve). (b) Seasonal cycle of surface temperature for the same four solutions as in (a). Note that the surface temperature in the idealized model is diagnosed from the computed thickness and the specified surface forcing. (c) Relaxation time to reach steady-state ice thickness from two different initial conditions in the MU71 model with $h_s = A_R = 0$ (black curves and circles) and in the idealized sea ice model (blue curves).

(i) When the surface is below the freezing temperature ($T_i < 0$), the upper boundary condition [**7**] with the linear temperature profile takes the form

$$k_i \frac{T_i}{h_i} = -F_{top}(t, T_i, \alpha_i). \qquad [10]$$

Since there is no surface ablation ($dh_T/dt = 0$), the ice thickness evolves as $dh_i/dt = d/dt\,(h_T - h_B) = -dh_B/dt$, and after inserting the linear temperature profile the lower boundary condition [**9**] becomes

$$L_i \frac{dh_i}{dt} = -k_i \frac{T_i}{h_i} - F_B. \qquad [11]$$

Inserting the surface temperature [**10**] into equation [**11**] shows that ice thickness evolves according to

$$L_i \frac{dh_i}{dt} = F_{top}(t, T_i, \alpha_i) - F_B. \qquad [12]$$

(ii) During surface ablation ($T_i = 0$), the temperature profile takes on a constant value of $\tilde{T} = \tilde{T}_{fr}$. Hence the upper boundary condition [**7**] takes the form

$$F_{top}(t, T_i, \alpha_i) = L_i \frac{dh_T}{dt}, \qquad [13]$$

and the lower boundary condition [**9**] becomes

$$-L_i \frac{dh_B}{dt} = -F_B, \qquad [14]$$

which together imply that ice thickness, $h_i = h_T - h_B$, evolves according to an equation identical to the case with the surface below the freezing temperature [**12**].

The steady-state surface temperature can be derived by inserting equation [**8**] into equation [**10**] to yield an algebraic solution for the case with $T_i < 0$, which can be combined with the ablation case ($T_i = 0$) as

$$T_i(t, h_i) = -\mathcal{R}\left[\frac{(1-\alpha_i)\,F_S(t) - F_0(t)}{-k_i/h_i - F_T(t)}\right]. \qquad [15]$$

Here the dependence of T_i on t and h_i has been explicitly indicated, and the ramp function $\mathcal{R}(x)$ is defined to be $\mathcal{R}(x) = 0$ if $x < 0$ and $\mathcal{R}(x) = x$ if $x \geq 0$. Note that the two surface boundary conditions in equation [**7**] are compactly embodied in the ramp function in equation [**15**]. The thickness evolution in both cases [**12**] can be written after inserting equation [**8**] as

$$L_i \frac{dh_i}{dt} = -(1-\alpha_i)F_S(t) + F_0(t) + F_T(t)T_i(t, h_i) - F_B. \qquad [16]$$

The sea ice model is fully contained in equations [**15**]-[**16**]. The results of this idealized ice thermodynamics model forced by specified surface and basal fluxes as in MU71 are shown in Fig. S2 (blue curves), which indicates that this approximate representation yields results in good agreement with the full numerical solution to the partial differential equation [**6**] in MU71 (cf. refs. 3, 4).

While most aspects of horizontal sea ice dynamics are neglected in this idealized treatment, in the coupled version of the model (equations [**1**]-[**4**] of the Research Report) we parameterize the net annual export of sea ice out of the central Arctic, most of which escapes through Fram Straight. Arctic sea ice has a residence time of roughly 3-12 years (5), with a net annual export of about 10% of the ice area (6). This continuous export makes the ice thickness somewhat more stable: to maintain thicker ice, a larger amount of new ice must be produced each year. We approximately account for this by adding to the ice thickness evolution [**16**] a decay term $-v_0 L_i h_i$, with $v_0 = 0.1$ yr^{-1}.

Atmosphere

In the presence of significantly different Arctic Ocean surface conditions, such as an exposed ocean mixed layer, the atmospheric energy fluxes into the surface are also expected to change significantly. This is particularly true for the downwelling longwave radiation which includes the effects of both horizontal atmospheric heat flux convergence and downward emission of absorbed upward longwave radiation due to the opacity of the atmosphere (i.e., the greenhouse effect). Here we use an idealized atmospheric model to account for changes in downwelling longwave radiation. This allows us to approximate $F_{top}(t, T, \alpha)$ over a wide range of climates. The derivation that follows is similar to previous treatments of two-stream radiative atmospheres (e.g., refs. 3, 7, 8).

Heat Flux Convergence. The meridional heat flux convergence averaged over 70°N–90°N is equivalent to a spatially averaged vertical flux of roughly $D = 100$ Wm^{-2} (9). Since the poleward heat flux in the atmosphere is related to transport of sensible and latent heat by eddies, it is often approximated in idealized climate models as being proportional to the meridional temperature difference (10–12), which is equivalent to assuming meridional effective diffusion of temperature as in typical atmospheric energy balance models (13–15). Although a destabilizing increase in atmospheric meridional heat flux into the Arctic may occur in response to warming due to factors including increased humidity (16–19), if the warming

is significant then reduced atmospheric heat transport is expected to be a principal damping mechanism (20). Here we follow the convention of setting the meridional heat flux to be proportional to the meridional temperature difference,

$$D(t,T) = k_D \Delta T_{merid}(t), \qquad [17]$$

where $\Delta T_{merid} = T_{south}(t) - T$ with T the simulated surface temperature in the Arctic and $T_{south}(t)$ the seasonally varying temperature south of the Arctic which is specified here from NCEP-NCAR reanalysis 1971-2000 climatological 1000mb atmospheric temperature (21) spatially averaged from the equator to 70°N. We use $k_D = 2.7$ Wm^{-2}/K, which optimizes the match to observed poleward heat transport (9) (although this parameterization leads to a model annual cycle in D that is somewhat exaggerated compared to observations).

Longwave Absorption. We use a vertically continuous dry energy balance atmospheric model. We approximate there to be no absorption of shortwave radiation in the atmosphere and no scattering of longwave radiation. Longwave radiation is absorbed and emitted in continuous vertical levels with an absorption cross section that is independent of wavelength, temperature, and pressure, and the radiative fields are solved using a two-stream approximation. We assume that the poleward atmospheric heat transport into the Arctic, $D(t,T)$, is distributed uniformly in optical height (3).

The intensity of a beam of radiation propagating vertically upward from Earth's surface will diminish with height z according to $dI/dz = -\rho(z)\kappa(z)I$, where $\rho(z)$ is the atmospheric density and $\kappa(z)$ is the extinction coefficient. This can be solved for intensity as a function of height,

$$I = I_0 \exp\left[-\int_0^z \rho(z')\kappa(z')dz'\right] = I_0 \exp[-\tau(z)], \qquad [18]$$

where I_0 is the intensity at the surface and the optical height is $\tau(z) \equiv \int_0^z \rho(z')\kappa(z')dz'$. We measure height using $\tau(z)$ instead of z, which has the advantage that $\kappa(z)$ and $\rho(z)$ are eliminated from the equations and the atmosphere can be approximately described by a single parameter, the total optical thickness $\tau_1 \equiv \tau(z \to \infty)$. Note that our use of optical height differs slightly from the standard convention of using optical depth, which is integrated from the top of the atmosphere downward. Regarding the physical meaning of the optical thickness τ_1, note that the fraction of longwave radiation emitted vertically from the surface that escapes to space is $\exp(-\tau_1)$. A slanted optical path in the atmosphere, $\delta\tau^*$, can be related to optical height according to $\delta\tau = \delta\tau^* \cos\theta$, where θ is the angle the path makes with the vertical (Fig. S3).

The intensity of longwave radiation in the atmosphere, $I(\tau,\theta,\phi)$, is a scalar field that depends on optical height and direction, with ϕ being the azimuthal angle (Fig. S3). We model the atmosphere as a grey material that absorbs a fraction $\delta\tau^*$ of the intensity passing through it and emits an equivalent fraction $\delta\tau^*$ of its blackbody radiation. The blackbody radiation of an air parcel can be computed from the Stefan-Boltzmann equation, $B(T_a) = \sigma T_a^4/\pi$, where T_a is the temperature of the air parcel and the factor π accounts for radiation occurring in every direction from a point source. This gives a change in intensity of $\delta I = -I\delta\tau^* + B\delta\tau^*$, which becomes the Schwarzschild equation when written in terms of optical height:

$$\cos\theta \frac{\partial I(\tau,\theta,\phi)}{\partial\tau} = -I(\tau,\theta,\phi) + B(\tau). \qquad [19]$$

Note that B is independent of angle since a blackbody emits radiation equally in all directions.

We assume horizontally uniform radiation from the surface and a horizontally homogenous atmospheric medium, which makes the intensity horizontally isotropic due to azimuthal symmetry, $I(\tau,\theta,\phi) = I(\tau,\theta)$. In thermal steady-state, this can be written as a vertically constant divergence of vertical net flux,

$$\frac{\partial}{\partial\tau}\int d\omega I(\tau,\theta)\cos\theta = \frac{D(t,T)}{\tau_1}, \qquad [20]$$

where we have defined the integral over all solid angles, $\int d\omega \equiv \int_0^\pi d\theta \int_0^{2\pi} \sin\theta d\phi$. We can rewrite the divergence condition [20] as an algebraic equation by equating it with the integral over all solid angles of the Schwarzschild equation [19]. Solving this for $B(\tau)$ and inserting this into the Schwarzschild equation [19] gives a single integro-differential equation for $I(\tau,\theta)$,

$$\cos\theta\frac{\partial I(\tau,\theta)}{\partial\tau} = -I(\tau,\theta) + \frac{1}{4\pi}\left[\frac{D(t,T)}{\tau_1} + \int d\omega I(\tau,\theta)\right]. \qquad [21]$$

The boundary conditions are that there is no downward longwave radiation at the top of the atmosphere ($\tau = \tau_1$),

$$I(\tau_1, \pi/2 \le \theta \le \pi) = 0, \qquad [22]$$

and that the upward radiative flux from the surface ($\tau = 0$) is $\sigma_0 + \sigma_T T$,

$$I(0, 0 \le \theta \le \pi/2) = \frac{\sigma_0 + \sigma_T T}{\pi}. \qquad [23]$$

The system [21]-[23] uniquely specifies atmospheric longwave radiation $I(\tau,\theta)$ given the poleward heat transport $D(t,T)$, atmospheric optical thickness τ_1, and surface temperature T.

Here we use a standard two-stream approximation to arrive at an analytical solution to the system [21]-[23]. Multiplying the Schwarzschild equation [19] by $\cos\theta$ and integrating over the upper and lower hemispheres (i.e., the upper and lower halves of an infinitesimal sphere surrounding a given point in the atmosphere) leads to

$$\frac{\partial}{\partial\tau}\int d\omega^\uparrow I(\tau,\theta)\cos\theta = -F^\uparrow(\tau) + \pi B(\tau), \qquad [24]$$

$$\frac{\partial}{\partial\tau}\int d\omega^\downarrow I(\tau,\theta)\cos\theta = F^\downarrow(\tau) - \pi B(\tau), \qquad [25]$$

where we have defined total upward and downward fluxes through a horizontal surface in the atmosphere,

$$F^\uparrow(\tau) \equiv \int d\omega^\uparrow I(\tau,\theta)\cos\theta, \qquad [26]$$

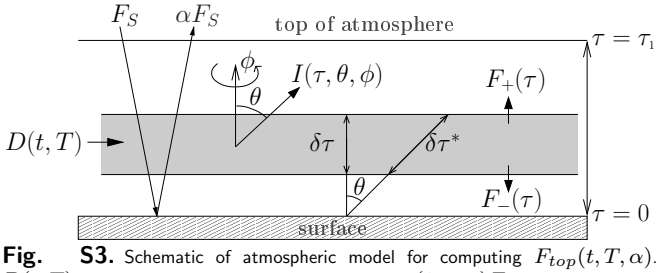

Fig. S3. Schematic of atmospheric model for computing $F_{top}(t,T,\alpha)$. $D(t,T)$ represents meridional heat transport, and $(1-\alpha)F_S$ is the amount of absorbed solar radiation. Longwave radiative intensity is represented by I and optical height is given as τ with $\delta\tau^*$ an optical path at angle θ to the vertical. Note that here the optical height increases upward, in contrast with the optical depth which increases downward and is typically used in radiative transfer calculations. The total upward and downward longwave radiative fluxes through a horizontal surface are $F_+(\tau)$ and $F_-(\tau)$, respectively. The model allows the surface incident longwave radiation to be represented as a function of outgoing surface longwave radiation (equation [34]).

$$F^{\downarrow}(\tau) \equiv -\int d\omega^{\downarrow} I(\tau,\theta)\cos\theta, \qquad [27]$$

and the integrals over solid angles in each hemisphere are defined as $\int d\omega^{\uparrow} \equiv \int_0^{\pi/2} d\theta \int_0^{2\pi} \sin\theta d\phi$ and $\int d\omega^{\downarrow} \equiv \int_{\pi/2}^{\pi} d\theta \int_0^{2\pi} \sin\theta d\phi$.

The type of two-stream approximation we employ, an exponential kernel approximation (sec. 2.4 of ref. 7), is equivalent to assuming that radiation propagates through the atmosphere only at one effective angle. This angle deviates from the vertical to account for the fact that in the exact solution radiation propagates in all directions. Upwelling radiation propagates along $\theta = \theta_{\text{eff}}$ and downwelling radiation propagates along $\theta = \theta_{\text{eff}} + \pi$. This assumption allows equations [**24**]-[**25**] to be written as

$$\cos\theta_{\text{eff}} \frac{\partial F^{\uparrow}(\tau)}{\partial \tau} = -F^{\uparrow}(\tau) + \pi B(\tau), \qquad [28]$$

$$\cos\theta_{\text{eff}} \frac{\partial F^{\downarrow}(\tau)}{\partial \tau} = F^{\downarrow}(\tau) - \pi B(\tau). \qquad [29]$$

Note that the negative sign from the definition of $F^{\downarrow}$ [**27**] is cancelled in equation[**29**] because $\cos(\theta_{\text{eff}} + \pi) = -\cos\theta_{\text{eff}}$.

Inserting the definitions [**26**]-[**27**] into the divergence condition [**20**] leads to

$$\frac{\partial}{\partial \tau}\left[F^{\uparrow}(\tau) - F^{\downarrow}(\tau)\right] = \frac{D(t,T)}{\tau_1}, \qquad [30]$$

which can be multiplied by $\cos\theta_{\text{eff}}$ and then equated with the sum of equations [**28**] and [**29**]. This allows us to write the divergence condition as an algebraic relation that can be directly solved for $B(\tau)$:

$$B(\tau) = \frac{1}{2\pi}\left[\frac{D(t,T)\cos\theta_{\text{eff}}}{\tau_1} + F^{\uparrow} + F^{\downarrow}\right]. \qquad [31]$$

Finally, inserting the definitions [**26**]-[**27**] into the boundary conditions [**22**]-[**23**] leads to

$$F^{\downarrow}(\tau_1) = 0, \qquad [32]$$

$$F^{\uparrow}(0) = \sigma_0 + \sigma_T T. \qquad [33]$$

Equations [**28**]-[**29**], [**31**] represent a system of two coupled first order linear ordinary differential equations, which can be solved subject to boundary conditions [**32**]-[**33**] to give the full vertical profiles of $F^{\uparrow}(\tau)$ and $F^{\downarrow}(\tau)$. Note that the temperature profile can be calculated from this solution using equation [**31**] and the Stefan-Boltzmann equation. From the full solution to the system [**28**]-[**29**], [**31**]-[**33**] (not shown), the surface downward longwave radiation is

$$F^{\downarrow}(0) = \frac{\sigma_0 + \sigma_T T}{1 + \frac{2\cos\theta_{\text{eff}}}{\tau_1}} + \frac{D(t,T)}{2}. \qquad [34]$$

The incident surface radiation includes half of the atmospheric heat convergence, $D(t,T)/2$, while the other half is emitted to space. This arises from the assumption that $D(t,T)$ is evenly distributed in optical height.

The choice of θ_{eff} can be optimized to match the exact solution of the system [**21**]-[**23**] given values of $D(t,T)$, τ_1, and $F^{\uparrow}(0) = \sigma_0 + \sigma_T T$. Salby (sec. 8.4.2 of ref. 8) finds that the effect of averaging over spectral bands suggests the value $\cos\theta_{\text{eff}} = \frac{3}{5}$. Goody and Yung (sec. 9.2.1 of ref. 7) derive an atmosphere similar to the system [**28**]-[**29**], [**31**], with $D(t,T) = 0$, by using a version of the two-stream approximation in which hemispheric isotropy is assumed: $I(\tau,\theta > \pi/2) = I_+$ and $I(\tau,\theta > \pi/2) = I_-$. This yields a result equivalent to letting $\cos\theta_{\text{eff}} = \frac{2}{3}$. Thorndike (3) derives an atmosphere analogous to the model derived here but with only vertically propagating radiation, arriving at a result equivalent to $\cos\theta_{\text{eff}} = 1$. We take the optical thickness τ_1 as the tunable parameter in the model, and we leave $\cos\theta_{\text{eff}}$ unspecified because it simply scales the optical thickness.

The net longwave radiation from the solution [**34**] is

$$F^{\uparrow}(0) - F^{\downarrow}(0) = \kappa_{LW}(\sigma_0 + \sigma_T T) - \frac{D(t,T)}{2}, \qquad [35]$$

where we have defined an atmospheric greenhouse factor as

$$\kappa_{LW} \equiv 1 - \frac{1}{1 + \frac{2\cos\theta_{\text{eff}}}{\tau_1}} = \frac{1}{1 + \frac{\tau_1}{2\cos\theta_{\text{eff}}}}. \qquad [36]$$

Note that $0 < \kappa_{LW} < 1$. This makes clear the effect of the atmospheric longwave radiation model: it mitigates surface longwave cooling by emitting some of the energy back to the surface, equivalent to reducing the surface upward longwave radiation by the factor κ_{LW}, and it adds energy associated with atmospheric heat flux convergence (i.e., net meridional heat transport into the Arctic). By reducing the surface net upward longwave radiation, the interactive atmospheric model weakens the stabilizing influence of outgoing longwave radiation on the ice/ocean system.

Grey two-stream atmospheres like the model used here can capture many of the basic features of radiative transfer in an approximate way. A thorough comparison of various types of two-stream approximations is discussed in Goody and Yung (sec. 2.4 of ref. 7).

The optical thickness of the atmosphere depends on water vapor, cloud particles, and greenhouse gases such as carbon dioxide. It is higher during summer than during winter because of increased water vapor and cloudiness. We specify the optical thickness seasonal cycle to follow observed Arctic cloudiness,

$$\kappa_{LW}(t) = \frac{1}{\tau_0 + \tau_c f_c(t)}, \qquad [37]$$

where $f_c(t)$ is the Arctic cloud fraction seasonal cycle specified from observations (22) and τ_0 and τ_c are chosen to give a sea ice seasonal cycle matching that computed using forcing from MU71 (cf. refs. 3, 23). This leads to a choice of $\tau_0 = 0.5$ and $\tau_c = 3.6$.

The actual energy flux at the top of the sea ice or exposed ocean mixed layer, $F_{top}(t,T,\alpha)$, includes components of sensible and latent heat fluxes in addition to downward and upward shortwave and longwave radiation. According to the observationally-based central Arctic values specified in MU71, the sensible and latent heat fluxes are small compared to the radiative fluxes, and here we effectively approximate the sensible and latent heat fluxes by incorporating them into the computed downwelling longwave flux. The longwave emissivities of ice and open water, both roughly 0.95–1, are here approximated to unity. Under these approximations, the total surface flux can be written

$$F_{top}(t,T,\alpha) = \kappa_{LW}(t)(\sigma_0 + \sigma_T T) - \frac{D(t,T)}{2} - (1-\alpha)F_S(t), \qquad [38]$$

where the downwelling shortwave radiation incident at the surface, $F_S(t)$, is specified from observations as in MU71. Inserting equation [**17**], we see that the full temperature dependence is linear, allowing us to write F_{top} [**38**] in the form of equation [**8**] with parameters

$$F_0(t) = \kappa_{LW}(t)\sigma_0 - \frac{k_D}{2} T_{south}(t) \qquad [39]$$

and

$$F_T(t) = \kappa_{LW}(t)\sigma_T + \frac{k_D}{2}. \qquad [40]$$

Ocean Mixed Layer

To allow the simulation of ice-free conditions, we include a representation of an ocean mixed layer which becomes exposed when all of the ice ablates. The mixed layer is represented as a thermodynamic reservoir with a characteristic depth of $H_{ml} = 50$m, in agreement with observations (24). The mixed layer temperature evolution is proportional to the net flux,

$$c_{ml} H_{ml} \frac{dT_{ml}}{dt} = (1 - \alpha_{ml})\, F_S(t) - F_0(t) - F_T(t) T_{ml} + F_B, \qquad [41]$$

with mixed layer heat capacity $c_{ml} = 4 \times 10^6$ Jm^{-3}K^{-1}. We use an open water albedo of $\alpha_{ml} = 0.2$, similar to previous studies (3, 25), to account for the presence of small amounts of thin ice in a largely ice-free Arctic Ocean. When the ice completely melts ($h_i = 0$), the ocean mixed layer temperature is evolved forward from $T_{ml} = 0$, and when the mixed layer cools back to $T_{ml} = 0$, the ice thickness is evolved once again starting from $h_i = 0$.

Coupled Model

The separate equations for T_{ml} and h_i can be combined, since only one is evolving at any given time. We define the energy per unit area in the system, E, to be equal to the sum of the latent heat content of the sea ice and the specific heat content of the ocean mixed layer (equation **[1]** in the Research Report). This allows the ice and ocean mixed layer components of the idealized model **[15]**-**[16]**, **[41]** to be expressed as equations **[2]**-**[3]** in the Research Report. The parameters $F_0(t)$ and $F_T(t)$, which are used to determine the surface energy flux, have values computed using the atmospheric model **[39]**-**[40]**. An imposed annually constant surface energy flux is included in equations **[2]**-**[3]** by replacing $F_0(t)$ with $F_0(t) - \Delta F_0$. Values for the parameters in equations **[1]**-**[4]** in the Research Report are given in Table S1. The standard case simulation with this model, illustrated in Fig. S2, produces central Arctic sea ice conditions in fairly good agreement with MU71.

Table S1. Descriptions and default values of model parameters. Time evolution t is measured in years while fluxes are measured in Wm^{-2}, which allows most dimensional parameters to be approximately of order unity but requires a non-conventional choice of units for energy per unit area E (written in Wm^{-2}yr), heat capacity $c_{ml}H_{ml}$, and latent heat L_i. For the three seasonally varying parameters, the annual mean value is given in the table; the monthly values starting with January are $F_0(t)$ = (120, 120, 130, 94, 64, 61, 57, 54, 56, 64, 82, 110) Wm^{-2}, $F_T(t)$ = (3.1, 3.2, 3.3, 2.9, 2.6, 2.6, 2.6, 2.5, 2.5, 2.6, 2.7, 3.1) Wm^{-2}K^{-1}, and $F_S(t)$ = (0, 0, 30, 160, 280, 310, 220, 140, 59, 6.4, 0, 0) Wm^{-2}.

Symbol	Description	Value
L_i	Latent heat of fusion of ice	9.5 Wm^{-3}yr
$c_{ml}H_{ml}$	Ocean mixed layer heat capacity times depth	6.3 Wm^{-2}yrK^{-1}
α_i	Albedo when surface is ice-covered	0.68
α_{ml}	Albedo when ocean mixed layer is exposed	0.2
k_i	Ice thermal conductivity	2 Wm^{-1}K^{-1}
F_B	Heat flux into bottom of sea ice or ocean mixed layer	2 Wm^{-2}
h_α	Ice thickness range for smooth transition from α_i to α_{ml}	0.5 m
v_0	Dynamic export of ice from model domain	0.1 yr^{-1}
$F_0(t)$	Temperature-independent surface flux (seasonally varying)	85 Wm^{-2}
$F_T(t)$	Temperature-dependent surface flux (seasonally varying)	2.8 Wm^{-1}K^{-1}
$F_S(t)$	Incident shortwave radiation flux (seasonally varying)	100 Wm^{-2}
ΔF_0	Imposed surface heat flux	0 Wm^{-2}

1. Maykut, GA, Untersteiner, N (1971) Some results from a time-dependent thermodynamic model of sea ice. J Geophys Res 76:1550–1575.
2. Feltham, DL, Untersteiner, N, Wettlaufer, JS, Worster, MG (2006) Sea ice is a mushy layer. Geophys Res Lett 33:L14501.
3. Thorndike, AS (1992) A toy model linking atmospheric thermal radiation and sea ice growth. J Geophys Res 97:9401–9410.
4. Semtner, AJ (1976) Model for thermodynamic growth of sea ice in numerical investigations of climate. J Phys Oceanogr 6:379–389.
5. Rigor, IG, Wallace, JM (2004) Variations in the age of Arctic sea-ice and summer sea-ice extent. Geophys Res Lett 31:L09401.
6. Kwok, R, Cunningham, GF, Pang, SS (2004) Fram strait sea ice outflow. J Geophys Res 109:C01009.
7. Goody, R, Yung, Y (1989) Atmospheric Radiation: Theoretical Basis (Oxford University Press), 2 edition.
8. Salby, ML (1996) Fundamentals of Atmospheric Physics (Academic Press), p 627.
9. Nakamura, N, Oort, AH (1988) Atmospheric heat budgets of the polar-regions. J Geophys Res 93:9510–9524.
10. Chen, D, Gerdes, R, Lohmann, G (1995) A 1-D atmospheric energy-balance model developed for ocean modeling. Theor Appl Climatol 51:25–38.
11. Thorndike, A (1999) in Ice Physics and the Natural Environment, eds Wettlaufer, JS, Dash, JG, Untersteiner, N (Springer-Verlag), pp 169–183.
12. Gildor, H, Tziperman, E (2001) A sea-ice climate-switch mechanism for the 100 kyr glacial cycles. J Geophys Res 106:9117–9133.
13. Budyko, MI (1969) The effect of solar radiation variations on the climate of the earth. Tellus 21:611–619.
14. Sellers, WD (1969) A global climate model based on the energy balance of the earth-atmosphere system. J Appl Meteor 8:392–400.
15. North, GR, Cahalan, RF, Coakley, Jr., JA (1981) Energy balance climate models. Rev Geophys Space Phys 19:91–121.
16. Alexeev, VA (2003) Sensitivity to CO_2 doubling of an atmospheric GCM coupled to an oceanic mixed layer: a linear analysis. Clim Dynam 20:775–787.
17. Hall, A (2004) The role of surface albedo feedback in climate. J Clim 17:1550–1568.
18. Winton, M (2006) Amplified Arctic climate change: What does surface albedo feedback have to do with it? Geophys Res Lett 33:L03701.
19. Held, IM, Soden, BJ (2006) Robust responses of the hydrological cycle to global warming. J Clim 19:5686–5699.
20. Winton, M (2008) in Arctic Sea Ice Decline: Observations, Projections, Mechanisms, and Implications, eds Bitz, C, DeWeaver, E (Am Geophys Union), in press.
21. Kalnay, E et al. (1996) The NCEP/NCAR 40-year reanalysis project. Bull Amer Meteor Soc 77:437–471.
22. Maykut, GA, Church, PE (1973) Radiation climate of Barrow, Alaska, 1962-66. J Appl Meteor 12:620–628.
23. Björk, G, Söderkvist, J (2002) Dependence of the Arctic Ocean ice thickness distribution on the poleward energy flux in the atmosphere. J Geophys Res 107:3173.
24. Morison, J, Smith, JD (1981) Seasonal-variations in the upper Arctic ocean as observed at T-3. Geophys Res Lett 8:753–756.
25. Hibler, WD (1979) A dynamic thermodynamic sea ice model. J Phys Oceanogr 9:815–846.

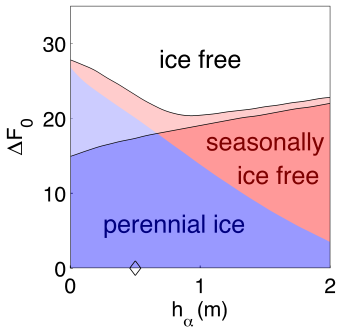

Fig. S4. Robustness of the results in Fig. 3 of the Research Report to parameter regime, illustrated here by varying the parameter governing the smoothness of the albedo transition (h_α). For each value of h_α, ranges of surface heating (ΔF_0) that give rise to stable solutions that are perennially ice-covered (blue region), seasonally ice-free (red region), or perennially ice-free (white region) are identified. The default parameter regime is indicated by a black diamond. Mixed shades indicate the overlap in regions where multiple stable solutions coexist, and the bifurcation curves marking the edges of this space are indicated by black curves. The lack of any purple region, which would indicate an overlap between red (seasonally ice-free) and blue (perennial ice), demonstrates that multiple states are not found with the warm state being seasonally ice-free, while the presence of light red and light blue regions shows that multiple states with the warm state being perennially ice-free are possible. The variation of other model parameters (not shown) leads to similar results. This indicates that although the size of the ΔF_0 range where multiple solutions coexist depends on h_α, both *(i)* the lack of a bifurcation threshold during the transition from perennial ice to seasonally ice-free conditions and *(ii)* the presence of multiple states and threshold behavior during the transition to perennially ice-free conditions are robust features of the model equations.

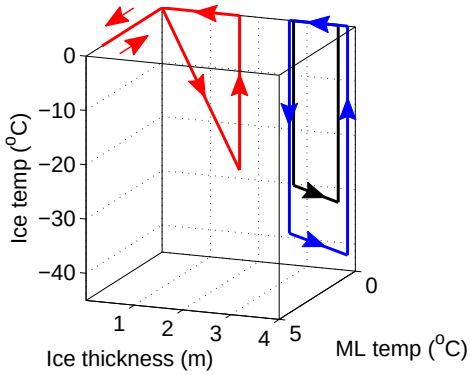

Fig. S5. Seasonal cycle of Arctic sea ice and ocean conditions simulated with the toy model of Thorndike (3). Seasonally varying solutions are plotted as closed curves in the three-dimensional model state space, which represents changes in sea ice thickness, sea ice surface temperature, and ocean mixed layer temperature. The standard case solution is indicated by the black curve. Thorndike found that when the specified atmospheric Arctic heat flux convergence D was increased, the model transitioned from perennially ice-covered to perennially ice-free conditions, with no stable seasonally ice-free solution possible. Rather than prescribing observed seasonally-varying forcing quantities, Thorndike assumed a step-function form for the forcing, with shortwave radiation and optical thickness taking on constant values during the summer and winter half-years. He found observationally consistent ice thickness with summer and winter optical thicknesses of 4.5 and 3, respectively (black curve). When we choose for these parameters instead 1.5 and 5, respectively, Thorndike's toy model simulates a relatively consistent approximation of the modern sea ice seasonal cycle (blue curve). Increasing D from 100 Wm^{-2} to 145 Wm^{-2} in this regime, however, produces a stable seasonally ice-free solution (red curve), in contrast to the results reported by Thorndike. A second stable state which is perennially ice-free exists for the solution indicated by the black curve, as discussed by Thorndike, but not for the solution shown here by the blue curve. A second stable state which is perennially ice-free does however exist for the solution indicated by the red curve. The coexistence in Thorndike's model of a stable seasonally ice-free solution and a stable perennially ice-free solution is consistent with the results presented here (Fig. 3 of the Research Report).